Int. J. Electrochem. Sci., 11 **(2016)** 5679 – 5690, doi: 10.20964/2016.07.98

International Journal of
ELECTROCHEMICAL
SCIENCE
www.electrochemsci.org

Prussian-Blue-Doped Super-Activated Carbon as a High Performance Supercapacitor Electrode Material

Qingyong Wang[1,2], *Yongjin Zou* [1,2,3,*], *Cuili Xiang*[1,2], *Hailiang Chu*[1,2], *Shusheng Liu*[1,2,*], *Erhu Yan*[1,2], *Fen Xu*[1,2], *Lixian Sun* [1,2], *Chengying Tang*[1,2]

[1]Guangxi Key Laboratory of Information Materials, Guilin University of Electronic Technology, Guilin 541004, P.R. China
[2]Guangxi Collaborative Innovation Center of Structure and Property for New Energy Materials, Guilin 541004, P.R. China
[3]Guangxi Experiment Center of Information Science, Guilin University of Electronic Technology, Guilin 541004, P.R. China
[*]E-mail: zouy@guet.edu.cn, 25245195@qq.com

Received: 11 April 2016 / *Accepted:* 1 May 2016 / *Published:* 4 June 2016

A Prussian-blue-doped super activated carbon (PB/SAC) nanocomposite was prepared by a simple reduction method under mild condition. Scanning electron microscopy, X-ray diffraction, Fourier-transform infrared spectroscopy, and transmission electron microscopy experiments revealed that PB nanoparticles were incorporated in the pores of the SAC. Cyclic voltammetry measurements indicated that the combination of PB and SAC significantly enhanced the capacity of the composite. The hybrid PB/SAC electrode yielded the maximum capacitance performance with a specific capacitance up to 263.7 F g^{-1} at a current density of 5 A g^{-1}. The rational combination of these two materials provides the devices with an extended voltage window of 0.8 V in acid solution. Cyclic stability measurements indicated that the specific capacitance of the PB/SAC nanocomposite electrode could retain 94.8% of its initial value over 1500 charge/discharge cycles. More significantly, the supercapacitors were designed to be low in cost and environmentally benign, and are therefore highly suitable for future energy storage systems.

Keywords: Supercapacitor; Super activated carbon; Prussian blue; Nanocomposite

1. INTRODUCTION

Energy-storage device research and development has flourished in recent years, spurred by the need to utilize energy generated intermittently by green sources, the longer autonomy and miniaturization of portable devices, and the search for low cost and improved performance in electric

cars. Supercapacitors, as an evolution of classic capacitors, have attracted extensive attention for future energy storage applications [1–6]. In fact, the energy and power densities of supercapacitors now lie between those of batteries and capacitors [7–12]. Supercapacitors may be categorized as electric double-layer capacitors (EDLCs) or pseudocapacitors, based on their different charge storage mechanisms. The former employ various kinds of carbon as electrode materials and the latter generally employ transition metal oxides or conducting polymers as electrode materials. EDLCs have high power densities with excellent reversibility and long cycle lives, whereas pseudocapacitors have much higher energy densities. To combine the advantages of double-layer capacitance and pseudocapacitance, hybrid capacitors that show high supercapacitance as well as excellent stability have been fabricated [13–16].

Charge storage in supercapacitors is mainly accomplished by the rapid accumulation of charge at the electrode/electrolyte interface under an external electric field. Hence, a highly accessible interface area with the electrolyte is desired to maximize capacitance. Activated carbon (AC), as a representative electrode material for EDLCs, has been widely used because of its high specific surface area and microporous structure, which can be generally acquired by the simple carbonization and activation of cheap and readily available natural biomass wastes or carbonaceous minerals [17–20]. AC also provides a satisfactory matrix for the doping of metal oxides or polymers because of its good adsorption properties and high electrical conductivity.

Prussian blue (PB) is a mixed-valence iron cyanide complex with a repeating unit of potassium or sodium ferrous ferricyanide hexacyano hexahydrate [7]. It has a cubic face-centered structure with Fe^{2+} and Fe^{3+} ions situated at alternate corners of the corner-shared octahedra, bridged by small conjugated cyanide (C≡N) anions. Different from typical battery materials which undergo phase changes during charge/discharge, cations can be reversibly inserted into or extracted from the open PB framework without altering the crystal structure or lattice parameters [7]. Thus, no phase changes occur at the electrode. The unique physical and electrochemical properties of PB have led to its exploration as a new type of pseudocapacitive material [21–26] which has high specific capacitance but poor cycling properties. To the best of our knowledge, however, Prussian-blue-doped activated carbon has not been well studied as a supercapacitor material.

In this study, a simple chemical method was used to fabricate PB/super-activated carbon (SAC) composites. The SAC was prepared by the activation of commercial AC, which afforded a much higher specific surface area. The PB/SAC system exhibited a fine synergy between the SAC and PB, with the obtained nanocomposite demonstrating a high specific capacitance and excellent cycle life.

2. MATERIALS AND METHODS

2.1. Preparation of SAC

All the starting materials were analytical grade and used without any further purification. Commercial AC and KOH were purchased from Guangdong Xilong Chemical Reagent Factory. To prepare the SAC, with constant electromagnetic stirring, AC (2 g) was added to a solution of KOH (8

g) in deionized water (70 mL), and the mixture was stirred for 2 h. Then, the solution was transferred into a 100 mL Teflon-lined autoclave and heated at 120 °C for 24 h. Then, the mixture was evaporated to dryness at 100 °C for 4 h under vacuum without further workup before placing it in a tube furnace at 750 °C under N_2 atmosphere for 4 h. The solids were collected on a filter and rinsed with distilled water. The SAC sample was finally dried at 80 °C in a vacuum oven for 24 h.

2.2. Preparation of SAC/PB binary nanocomposites

The detailed procedure is as follows. $FeCl_2$ (50 mg) was dissolved in alcohol (20 mL); SAC (50 mg) was added and the mixture was ultrasonicated for 0.5 h. Subsequently, a solution of $K_3[Fe(CN)_6]$ (70 mg) in deionized water (4 mL) was added to the above solution dropwise. The suspension was further agitated for 12 h, and the precipitate was filtered and washed with deionized water and alcohol thoroughly. The sample was then dried in a vacuum oven at 80 °C for 24 h. To obtain different loadings of PB on the SAC, the weight of $FeCl_2$ was varied from 0.05 to 0.10 and 0.15 g, corresponding to $FeCl_2$/SAC feed ratios of 1, 2, and 3 by weight. Figure 1 shows the simple schematic illustration of the PB/SAC preparation. PB was chemically synthesized under similar conditions without the addition of SAC.

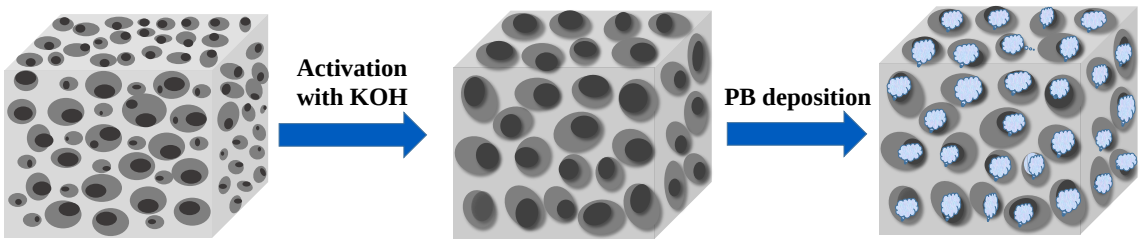

Figure 1. Schematic illustration of the fabrication of the PB/SAC nanocomposite.

2.3. Preparation of the electrodes

The synthesized PB/SAC composite-modified electrodes were prepared as follows: 2 mg of PB/SAC powder was suspended in 5 mL of dimethylformamide (DMF) under sonication for 30 min. The suspension (5 μL) of PB/SAC in DMF was drop-coated onto the surface of a prepared glassy carbon electrode (GCE) and then dried under an infrared lamp.

2.4. Instruments and analysis

Fourier-transform infrared (FTIR) spectra of all the samples were recorded using a Bruker Equinox 55 spectrometer. The morphologies were determined on a Hitachi S-4800 field-emission scanning electron microscope (SEM) with an accelerating voltage of 0.5–30 kV and a JEOL JEM-2000EX transmission electron microscope (TEM) with an accelerating voltage of 20 kV. The specific surface areas of the samples were measured by N_2 adsorption at 196 °C using the Brunauer-Emmett-

Teller (BET) method (Autosorb iQ2, Quantachrome Instruments, USA). The samples were degassed at 150 °C until the vacuum pressure was below 10^{-4} Pa. The crystal structures of the samples were examined using a Philips 1820 powder X-ray diffractometer (XRD).

Electrochemical measurements were performed using an IM6e potentiostat (ZAHNER-Elektrik, Kronach, Germany). All experiments were carried out with a conventional three-electrode system in 1.0 M KCl (pH = 3). The working electrode was a GCE (3 mm diameter). Prior to each experiment, the GCE was pretreated with established method [10].

3. RESULTS AND DISCUSSION

3.1 Characterization of PB/SAC

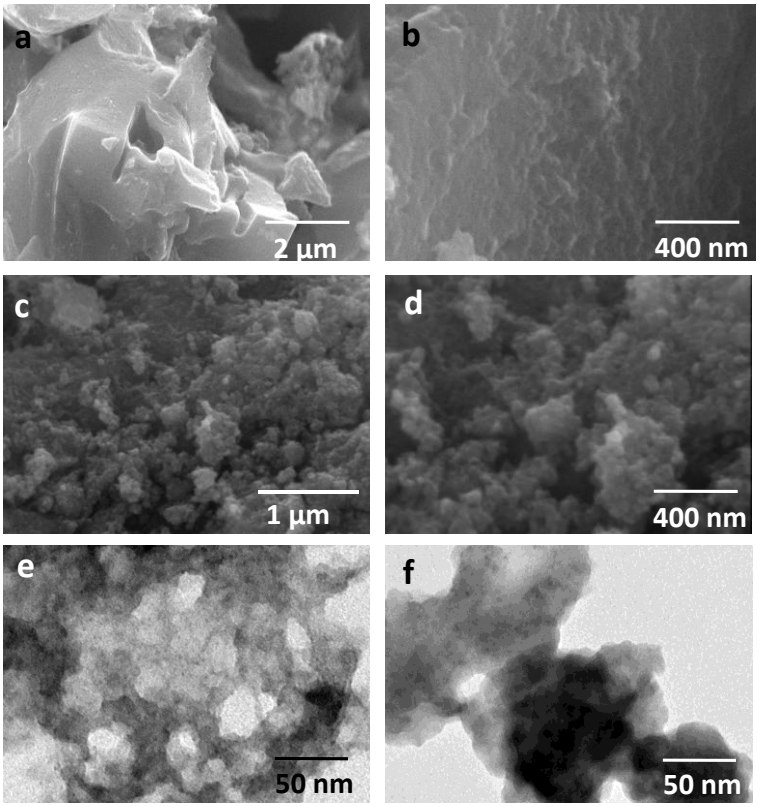

Figure 2. SEM images of (a,b) SAC and (c,d) PB/SAC. TEM images of (e) SAC and (f) PB/SAC.

Figure 2 shows the SEM and TEM images of SAC and the PB/SAC nanocomposites. The SAC sample in Fig. 2a and 2b consists of irregular granules with typical edge and corner features. As described in the experimental section, a KOH hydrothermal treatment process was used to obtain a more regular and mesoporous tunnel structure than is available in commercial AC powders. In the SEM images of the composite, PB nanoparticles with dimensions of 50–100 nm are anchored on the SAC matrix, covering nearly the whole particle surface (Fig. 2c, d). The TEM images (Fig. 2e, f) further approve that PB nanoparticles are incorporated in the SAC pore canals.

XRD patterns of the composite are shown in Fig. 3. Eight diffraction peaks at 2θ = 17.4, 24.7, 35.2, 39.5, 43.5, 50.6, 53.9, and 57.1° are easily found in the XRD patterns of the PB, which are corresponding to (200), (220), (400), (420), (422), (440), (600), and (620) planes of the face-centered-cubic phase of PB [2,27]. These peaks can also be found in the pattern of PB/SAC, which indicates that PB was successfully deposited on the SAC. For the SAC, a broad peak around 25° is observed, indicating its basically amorphous structure.

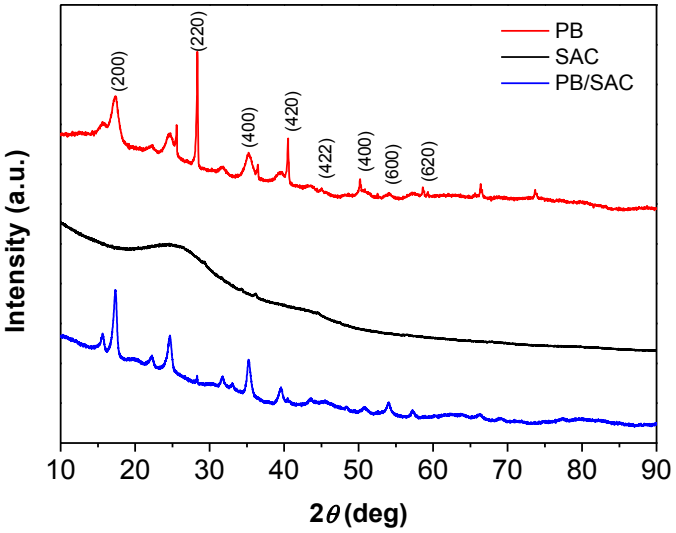

Figure 3. XRD patterns of the PB, SAC, and PB/SAC composite.

Figure 4 shows the FTIR spectra of the as-synthesized powders. In the spectra of PB, the absorption at 2090 cm^{-1} can be attributed to the CN stretching vibrations combined with Fe in the +2 oxidation states [2]. While the absorption band at 500 cm^{-1} should be ascribed to the metal–carbon–nitrogen bending modes in PB. These bands can also be observed in the PB/SAC spectrum. In addition, the absorption bands near 3430 and 1610 cm^{-1}, attributable to the O–H stretching and H–O–H bending modes, respectively, indicate the presence of interstitial water in the samples [17,28,29].

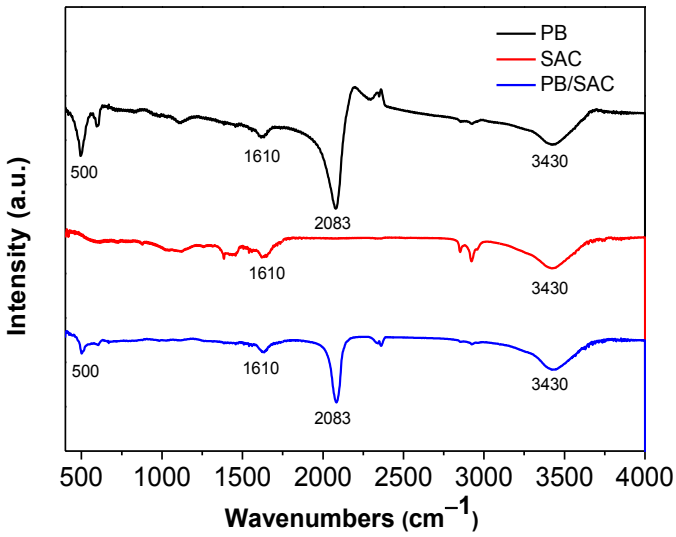

Figure 4. FTIR spectra of the as-synthesized materials.

Fig. 5 shows the N_2 adsorption/desorption isotherms and Barrett–Joyner–Halenda (BJH) pore-size distribution plots. The BET surface areas are 10, 934, 3000, and 479 $m^2\ g^{-1}$ for the PB, AC, SAC, and PB/SAC samples, respectively. SAC has a much higher surface area than AC (Fig. 5a), indicating the large number of porous structures formed after activation. Meanwhile, in the composite, the addition of PB to SAC decreases the surface area by blocking the pores of the SAC; this result is further confirmed by the pore-size distribution. The isotherm obtained for PB/SAC is characteristic of a type IV loop which confirms the mesoporous structure. The pore-size distribution plots for the SAC and PB/SAC present sharp peaks near 13.1 and 2.6 nm, respectively (Fig. 5b), which demonstrate that the incorporation of PB particles into the SAC pores decreases the pore size in the composite.

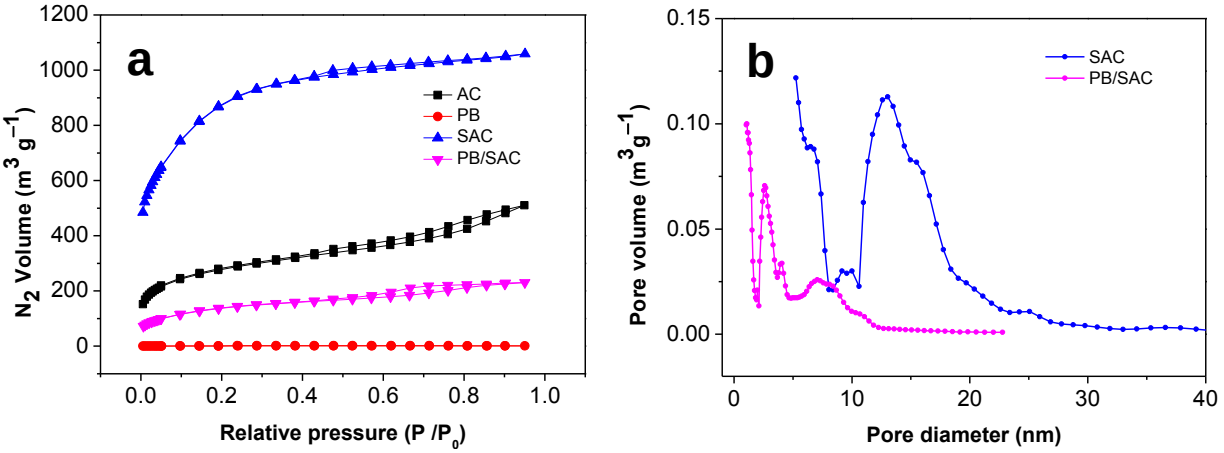

Figure 5. (a) N_2 adsorption/desorption isotherms of the AC, SAC, PB, and PB/SAC composite, and (b) BJH pore-size distribution curves for the SAC and PB/SAC composite.

3.2 Electrochemical performance

To ascertain the potential of the PB/SAC hybrid nanostructure as a supercapacitor electrode, its electrochemical properties were investigated by cyclic voltammetry (CV) and galvanostatic charge/discharge (GCD) measurements. The effects of the PB content on the electrochemical performance of the PB/SAC electrode were examined by preparing $FeCl_2$/SAC composites with different feed ratios (1:1, 1:2, and 1:3). Fig. 6 shows the typical CV curves for the different PB/SAC electrodes at a scan rate of 10 mV s^{-1} from −0.2 to 0.6 V. The specific capacitance is proportional to the area under the CV curve, and the shape of the curve reveals that the capacitance characteristics result from double-layer capacitance derived from the SAC as well as pseudocapacitance derived from the PB. The 1:2 PB/SAC electrode showed a stronger current response and higher double-layer capacitance and pseudocapacitance than the 1:1 and 1:3 composites, which may result from the smaller size of the PB nanoparticles and more uniform distribution of PB on the surface of the SAC. Subsequent experiments were based on this material.

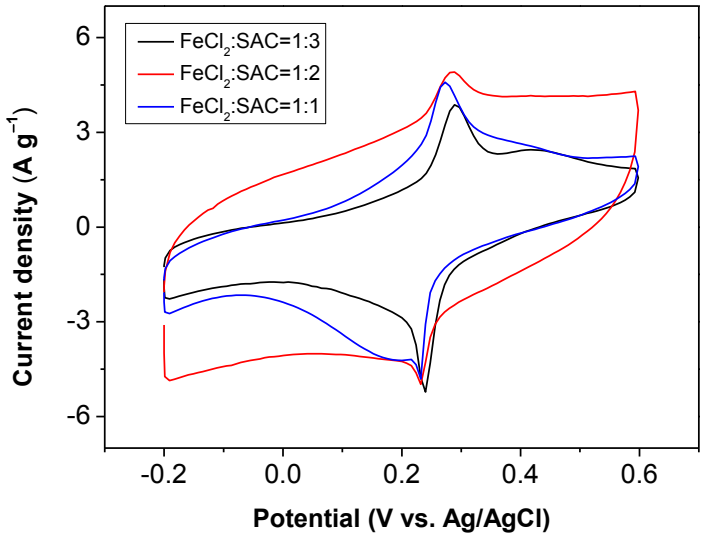

Figure 6. CV curves of the PB/SAC composite electrodes with different $FeCl_2$:SAC ratios at a scan rate of 10 mV s^{-1} in 1.0 M KCl (pH = 3).

Figure 7 shows the CV curves of the PB, SAC, and PB/SAC electrodes obtained at a scan rate of 10 mV s^{-1}. The specific capacitance values calculated from the CV curves are 188.7, 147.5, and 306.3 F g^{-1}, respectively. The CV curves of the SAC electrode are nearly rectangular in shape, indicating ideal EDLS behavior. It is easily observed that the area of the CV loops of PB/SAC is much larger than that of the single component, which indicates a higher specific capacitance. The PB/SAC electrode shows a pair of well-defined symmetric redox peaks, which indicate a good reversibility.

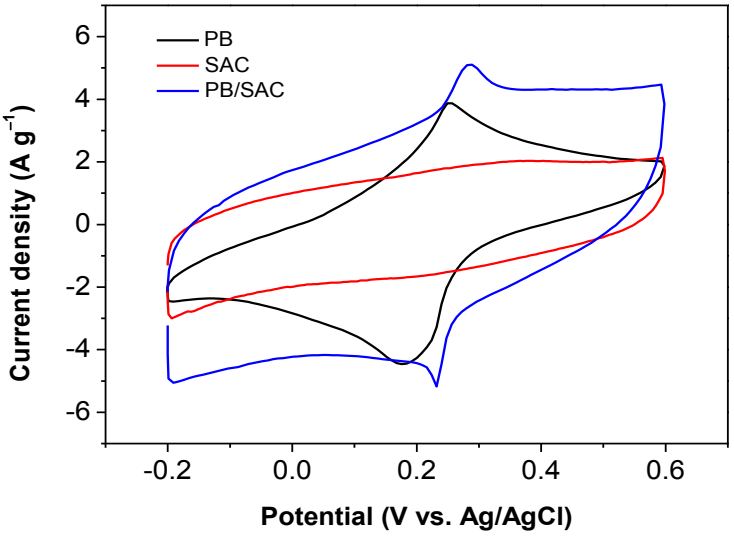

Figure 7. CV curves of the PB/SAC, SAC, and PB electrodes at a scan rate of 10 mV s^{-1} in 1.0 M KCl (pH = 3).

The CVs of PB/SAC at various scan rates were also investigated. As shown in Figure 8, when the scan rate is increased from 10 to 250 mV s^{-1} in an acidic 1.0 M KCl aqueous electrolyte, the peak

current densities increase nearly linearly with the scan rates, indicating a rapid redox reaction and high-rate capability of PB/SAC.

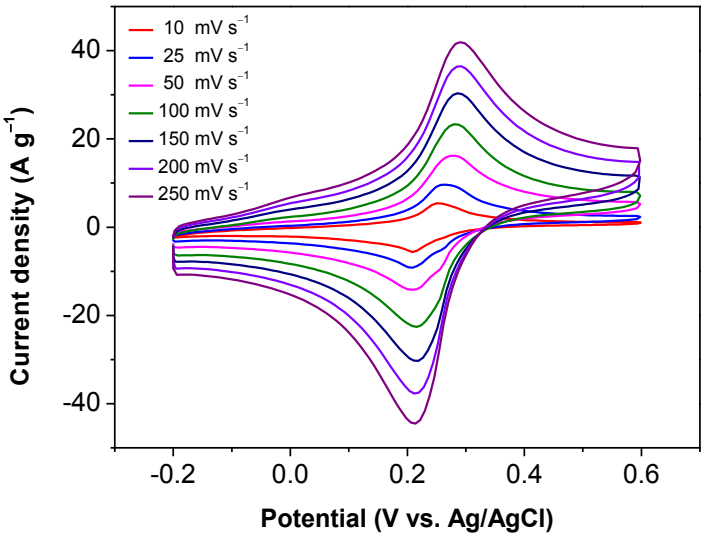

Figure 8. CV curves of the PB/SAC electrode at various scan rates in 1.0 M KCl (pH = 3).

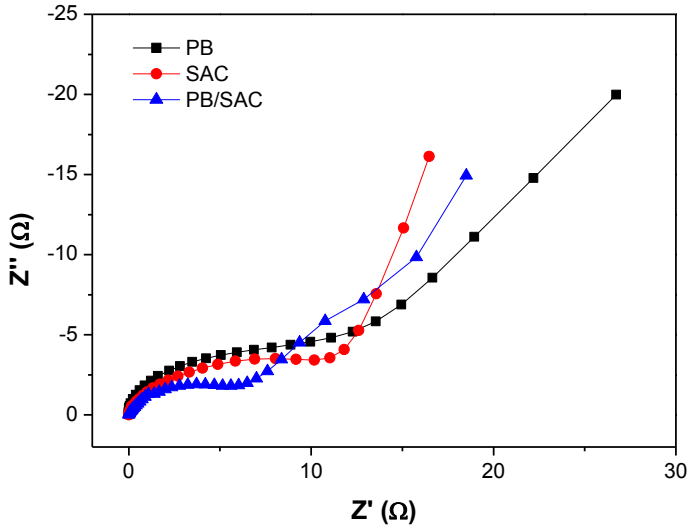

Figure 9. Nyquist plots of the as-synthesized materials.

Figure 9 shows the resulting Nyquist plots of the EIS spectra for the PB, SAC, and PB/SAC composite electrodes. All the Nyquist plots are composed of an inconspicuous semicircle in the high-frequency region and a straight line in the low frequency region. The calculated charge-transfer resistance values for the PB/SAC, SAC, and PB electrodes were 4.8, 5.4, and 6.5 Ω, respectively. The PB/SAC electrode had the lowest charge-transfer resistance value, indicating PB/SAC has good conductivity, which is because PB particles are embedded into the SAC pores.

Figure 10 shows the charge/discharge curves for the PB, SAC, and PB/SAC electrodes at a current density of 5 A g^{-1}. The specific capacitance values derived from the discharge curves were calculated to be 91.2, 107.8, and 263.7 F g^{-1} for the PB, SAC, and PB/SAC electrodes, respectively.

These are consisted with the results obtained by CV measurements. The charge/discharge curves of PB, SAC, and PB/SAC are almost symmetrical, indicating good capacitive behavior. The observed deviation in linearity is mainly due to the presence of pseudocapacitive PB. The IR drop of the PB/SAC is lower than the single component electrode, indicating internal resistance of PB/SAC is lower than the single component electrode. A comparison of the specific capacitance of the PB/SAC electrode with literatures is shown in Table 1. The PB/SAC electrode has larger specific capacitance than those of most previously reported results.

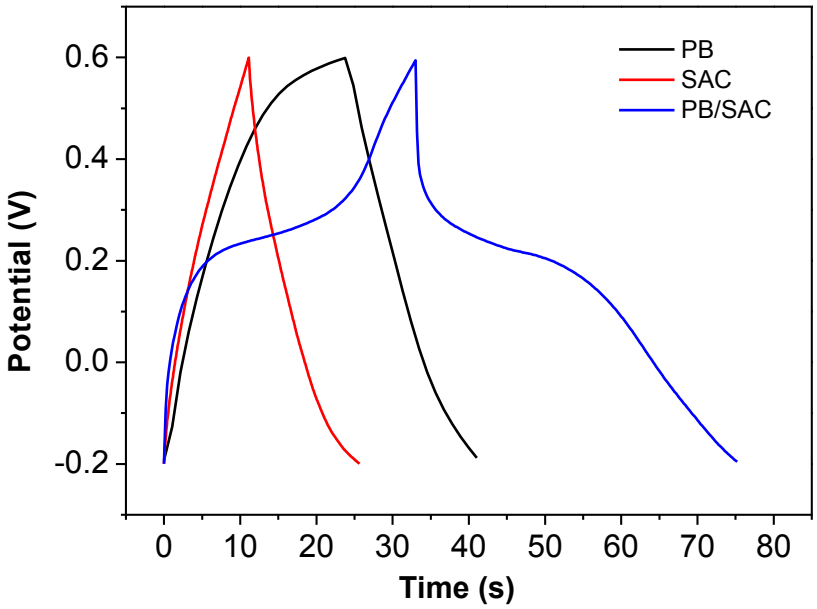

Figure 10. Charge/discharge curves the as-synthesized electrodes at 5 A g^{-1}.

Table 1. Gravimetic specific capacitance of the PB/SAC electrode compared with literatures

Sample	Capacitance measured at (A g^{-1})	Specific capacitance (F g^{-1})	Electrolyte	Reference
PB–rGO	1	195.6	KNO_3	[2]
MnHCF–MnO_2	0.5	225.6	Na_2SO_4	[30]
NiHCF–MnO_2	1	199.6	Na_2SO_4	[31]
MnO_2–PANI–GO	5	276	Na_2SO_4	[32]
MnO	0.125	100	Na_2SO_4	[33]
MnO_2/Ag	0.3	198.9	Na_2SO_4	[34]
Z-900	5	214	H_2SO_4	[35]
α-Fe_2O_3	0.5	249	KOH	[36]
RGO/KMn_8O_{16}	0.2	222.3	Na_2SO_4	[37]
PB/SAC	5	263.7	KCl	This work

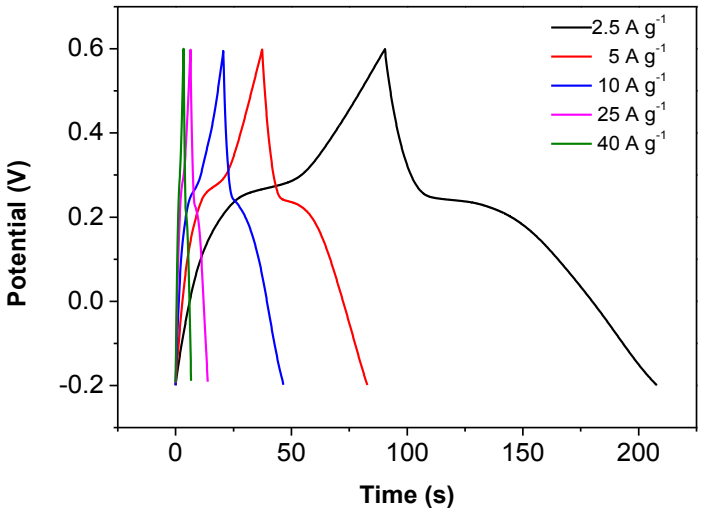

Figure 11. Galvanostatic charge/discharge curves of PB/SAC electrode at different densities of 2.5, 5, 10, 25 and 40 A g^{-1}.

The GCD curves at current densities of 2.5, 5, 10, 25, and 40 A g^{-1} are shown in Fig. 11. The triangular shapes of the GCD curves indicate good reversibility and capacitive performance during charging/discharging. The PB/SAC composite preserves 46.5% of its initial specific capacitance value as the current density is increased from 2.5 to 40 A g^{-1}, indicating its good high-rate capability .

To know the applicability of the PB/SAC hybrid supercapacitor, the cyclic stability (Fig. 12) is carried up to 1500 cycles at current density of 5 A g^{-1}. This PB/SAC electrode shows an excellent characteristic of recycling charge/discharge performance with relatively high capacitance value of 249.3 F g^{-1} after 1500 cycles, about 94.8% of the discharge capacitance of the initial cycle, reflecting the PB/SAC electrode has a good electrochemical stability.

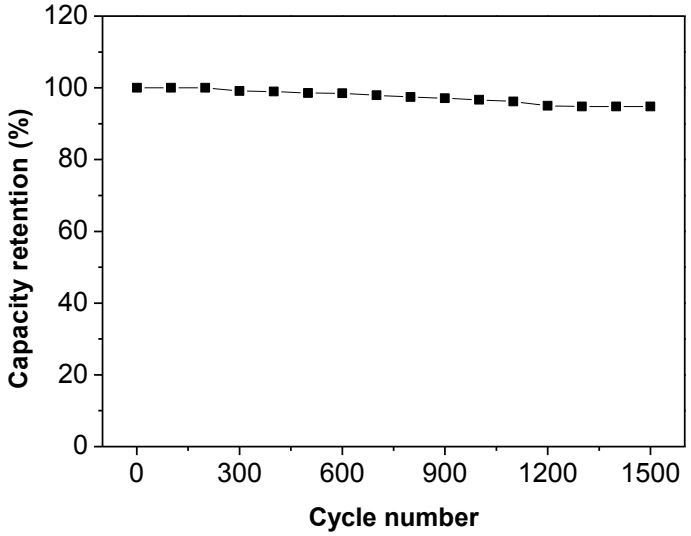

Figure 12. Cycling behavior of the PB/SAC electrode over 1500 cycles at a current density of 5 A g^{-1}.

4. CONCLUSIONS

In summary, PB/SAC nanocomposites were prepared by in-situ chemical reduction and used as supercapacitor electrode materials. The PB/SAC composite exhibits both double-layer capacitance and pseudocapacitance behaviors. It demonstrates excellent cyclic stability, with 94.8% capacitance retention for up to 1500 cycles, and provides a maximum specific capacitance of 263.7 F g^{-1} at a current density of 5 A g^{-1}. Therefore, we believe that the PB/SAC nanocomposite is a potential material to design high-performance supercapacitors.

ACKNOWLEDGEMENTS
Financial supports from the NSFC (U1501242, 51561006, 51261005, 51461010, 51401059, 51361005, 51371060, and 51461011), the Guangxi Natural Science Foundation (2014GXNSFAA118318, 2014GXNSFBA118240, and 2015GXNSFAA139282), and the Innovation Project of Guangxi Graduate Education (YCSZ2015153) are acknowledged.

References

1. N. Campagnol, V.R. Romero, W. Deleu, L. Stappers, K. Binnemans, D.E. De Vos, J. Fransaer. *ChemElectroChem*, 1(2014) 1182–1188.
2. M. Luo, Y. Dou, H. Kang, Y. Ma, X. Ding, B. Liang, L. Li. *J. Solid State Electrochem*, 19(2015) 1621–1631.
3. L. Yuan, C. Wan, L. Zhao. *Int. J. Electrochem. Sci*, 10(2015) 9456–9465.
4. L.L. Zhang, X.S. Zhao. *Chem. Soc. Rev.*, 38(2009) 2520–2531.
5. A.S. Adekunle, A.M. Farah, J. Pillay, K.I. Ozoemena, B.B. Mamba, B.O. Agboola. *Colloids Surf., B*, *95*(2012) 186–194.
6. M. Lin, J. Yang, M. Cho, Y. Lee. *Macromol. Res.*, *19*(2011) 673–678.
7. K.H. Park, D.Y. Choi, J.H. Park, C. Kim, T.Y. Kim, J.W. Lee. *Int. J. Electrochem. Sci*, 11(2016) 1472–1481.
8. S. Ghasemi, S.R. Hosseini, P. Asen. *Electrochim. Acta*, *160(*2015)337–346.
9. Z. H. Liu, G. F. Zhang, Z. Chen, B. Qiu, D. Tang. *Microchim. Acta*, *181*(2014)581–588.
10. Y.Zou, J. Cheng, C. Xiang, H. Chu, S. Qiu, F. Xu, L. Zheng. *Int. J. Electrochem. Sci*, 10 (2015)4626–4636.
11. R. Koncki. *Crit. Rev. Anal. Chem.*, *32*(2002) 79–96.
12. G. Lai, H. Zhang, A. Yu, H. Ju. *Biosens. Bioelectron*, *74*(2015) 660–665.
13. Q. Zhang, L. Zhang, J. Li. *Electrochim. Acta*, *53*(2008) 3050–3055.
14. L. M. Chen, Q. Y. Lai, Y. J. Hao, Y. Zhao, X. Y. Ji. *J. Alloys Compd.*, *467*(2009) 465–471.
15. N. H. Basri, M. Deraman, M. Suleman, N. S. M. Nor, B. N. M.Dolah, M. I. Sahri, S.A. Shamsudin. *Int. J. Electrochem. Sci*, *11*(2016)95–110.
16. C. K. Sim, S. R. Majid, N. Z. Mahmood. *Int. J. Electrochem. Sci*, *10*(2015)10157–10172.
17. I.I.G. Inal, S.M. Holmes, A. Banford, Z. Aktas. *Applied Surface Science*, *357*(2015)696–703.
18. J. Chang, Z. Gao, X. Wang, D. Wu, F. Xu, X. Wang, K. Jiang. *Electrochim. Acta*, *157*(2015) 290–298.
19. A. M. Farah, N. D. Shooto, F.T. Thema, J.S. Modise, E.D. Dikio. *Int. J. Electrochem. Sci.*, *7* (2012)4302–4313.
20. E. Nossol, A.J. Zarbin. *Energy Mater. Sol. Cells*, *109*(2013)40–46.
21. Y.Yue, Z.Zhang, A.J. Binder, J. Chen, X. Jin, S. H. Overbury, S .Dai. *ChemSusChem*, 8(2015)177–183.
22. X. Tuo, B. Li, C. Chen, Z. Huang, H. Huang, L. Li, X. Yu. *Synth. Met.*, 213(2016) 73–77.

23. L. Benhaddad, J. Gamby, L. Makhloufi, A. Pailleret, F. Pillier, H. Takenouti. *J. Power Sources*, 307(2016)297–307.
24. J. H. Shim, J. S. Lee, G. S. Cha, H. H. Nam. *Bull. Korean Chem. Soc.*, 31(2010)1583–1588.
25. S. Faraji, F. N. Ani. *Renewable Sustainable Energy Rev.*, 42(2015) 823–834.
26. R. S. Hastak, P. Sivaraman, D. D. Potphode, K. Shashidhara, A. B. Samui. *Electrochim. Acta*, 59(2012)296–303.
27. L. Benhaddad, J. Gamby, L. Makhloufi, A. Pailleret, F. Pillier, H. Takenouti. *J. Power Sources*, 307(2016)297–307.
28. J. Zhang, J. He, W. Xu, L. Gao, Y. Guo, W. Li, C. Yu. *Microchim. Acta*, 156(2015)45–52.
29. A. M. Farah, F.T. Thema, E.D. Dikio. *Int. J. Electrochem. Sci*, 7(2012)5069–5083.
30. Y. Wang, H. Zhong, L. Hu, N. Yan, H. B Hu, Q. W. Chen, *J. Mater. Chem. A* 1(2013)2621–2630.
31. Y. Wang, Q. W. Chen, *ACS Appl. Mater. Interfaces*, 6(2014) 6196–6201.
32. G. Han, Y. Liu, L. Zhang, E. Kan, S. Zhang, J. Tang, W. Tang, *Sci. Rep.*, 4(2014)4924 (7 page).
33. Y.Q. Ding, J.H. Yang, G.Z. Yang, P. Li, *Ceram. Int.*, 41 (2015) 9980–9987.
34. S. Lu, D. Yan, L. Chen, G. Zhu, H. Xu, A. Yu, *Mater. Lett.*, 168 (2016) 40–43.
35. W. Chaikittisilp, M. Hu, H. Wang, H. S. Huang, T. Fujita, K. C. W. Wu, K. Ariga, *Chem. Commun.*,48(2012) 7259–7261.
36. X. Zheng, X. Yan, Y. Sun, Y. Yu, G. Zhang, Y. Shen, Y. Zhang, *J. Colloid Interface Sci.*, 466(2016)291–296.
37. H. Guan, W. Dang, G. Chen, C. Dong, Y. Wang, *Ceram. Int.*, 42(2016)5195-5202.